



Modeling of the scattering response of particulate obscurant clouds



T.I. Zohdi

Department of Mechanical Engineering, University of California, Berkeley, CA 94720-1740, USA

ARTICLE INFO

Article history:

Received 29 November 2014

Accepted 2 December 2014

Keywords:

Obscurants

Discrete elements

Energy propagation

ABSTRACT

Obscurants are often clouds of dispersed particulate materials whose purpose is to mask a given object. The objective of this paper is to develop a simple discrete-ray/discrete-particle model in order to enable rapid assessment of the response of an obscurant cloud to an incoming high-frequency beam. The beam is decomposed into a set of discrete rays and the obscurant is represented by a discrete set of scattering particles. Ray-tracking is used to calculate the transient propagation of the rays and the absorption of energy by the particles. Examples are given, comprised of concentrated incident beams, their propagation into the obscurant cloud, and the subsequent reflection and transmitted aggregate response. Basic system trends are computed, varying the randomly dispersed particle shapes from spherical to oblate objects, which correlate the total amount of volume and surface area material available to interact with the beam and the overall scattering response. This allows further correlation of the obscurant cloud performance to the weight of the material, which is important for portable containers of dispersible obscurants, such as smoke grenades. Specifically, the model allows for rapid quantification of the modest reduction of scattering efficiency of flakes, relative to spheres, but which have significantly less weight than spheres. Thus, there is a trade-off between the weight of the dispersed system and its scattering efficiency.

© 2014 Elsevier Ltd. All rights reserved.

1. Introduction

Obscurants, such as smoke, have been used throughout the ages to mask the presence of objects. The objective of this work is to develop a discrete-ray/discrete-particle model to rapidly calculate the scattering of a high-frequency beam encountering a cloud of particles comprising an obscurant.¹ One key motivating application for this work is optimization and control of released obscurants to mask incoming signals which may be used to locate the object being obscured. The full sequence of events for release of a cloud of packed obscurant particles, for example from a grenade or canister, begins with an initiated shock wave that rapidly rips open the container (typically a lightweight hardened cylinder of cardboard) which releases a packed powder of particles forming a cloud. In this paper we are primarily interested in the response of the cloud to incoming optical disturbances, and the effect of the shapes of the particles on the overall optical response. Also, because the weight of the canisters is of importance when they are carried, the question of whether one can utilize less weight-intensive flakelike materials, as opposed to powders containing heavier spherical powders is relevant. Thus, one component of interest in the present study is to develop a simple and fast computational tool, which captures the essential physics of incidence,

E-mail address: zohdi@me.berkeley.edu

¹ The present discrete-rate/discrete-particle model is a simple alternative to a full-blown continuum description employing Maxwell's equations.

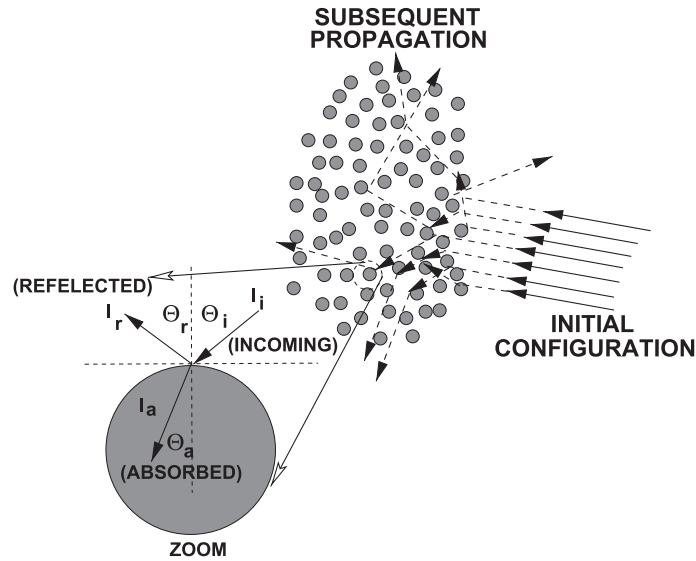


Fig. 1. A high-frequency pulse applied to a dispersed material, with a zoom on a reflection and absorption of an individual incoming ray and an individual particle.

absorption and reflection, and then use it to perform parameter studies on how the shape of the obscurant particles affect the overall response of a cloud to an incoming pulse of optical energy. In this work, we do not consider the problem of the dynamics of the disperse particles and the heat transfer, due to the interaction between the shock wave and the packed particles (Cabalo, Schmidt, Wendt, & Scheeline, 2002; Gregoire, Sturtzer, Khasainov, & Veyssiere, 2009; Hoover & Hoover, 2009; Kudryashova et al., 2011), which is beyond the scope of the present work. For studies of the evolution of heat and the dynamics (movement) of the particles, we refer the reader to Zohdi (2004, 2005, 2006a, 2006b, 2007, 2010, 2012a, 2012b, 2013, 2014). This entails an analysis of the dynamics of particulate clouds and flows, related to granular flow models, as well as coupled fluid-particle interaction problems, which are found in Duran (1997), Pöschel and Schwager (2004), Onate, Idelsohn, Celigueta, and Rossi (2008), Onate, Celigueta, Idelsohn, Salazar, and Suarez (2011), Rojek, Labra, Su, and Onate (2012), Carbonell, Onate, and Suarez (2010), Labra and Onate (2009), Avci and Wriggers (2012), Leonardi, Wittel, Mendoza, and Herrmann (2014), Cante et al. (2014), Rojek (2014), Onate et al. (2014) and Bolintineanu et al. (2014).

In order to enable the ability to study the particulate cloud systems, we develop a discrete-ray/discrete-particle model for the characterization of the response of an obscurant cloud to a concentrated beam of high-frequency energy is the key objective of this work. Specifically, the interest here is on behavior of initially coherent beams (Fig. 1), composed of multiple collinear (collimated) rays (initially forming a planar wave front), where each ray is a vector in the direction of the flow of optical energy (the rays are parallel to the initial wave's propagation vector). It is assumed that the particles and surface features are at least an order of magnitude larger than the wavelength of the incident radiation, therefore "geometrical" ray tracing theory is applicable, and is well-suited for the systems of interest. Ray-tracing is a method that is employed to produce rapid approximate solutions to wave-equations for high-frequency/small-wavelength applications where the primary interest is in the overall propagation of energy.² Essentially, ray-tracing methods proceed by initially representing wave fronts by an array of discrete rays. *Thereafter, the problem becomes one of a primarily geometric character*, where one tracks the changing trajectories and magnitudes of individual rays which are dictated by the reflectivity and the Fresnel conditions (if a ray encounters a material interface). Ray-tracing methods are well-suited for computation of scattering in complex systems that are difficult to mesh/discretize, relative to procedures such as the Finite Difference Time Domain Method or the Finite Element Method. For review of the state-of-the-art in industrially-oriented optics, see Gross (2005). As alluded to, because of the complex, discrete, randomly dispersed particulate microstructure of an obscurant cloud, this type of system is extremely difficult to simulate using continuum-based methods, such as the Finite Difference Time Domain Method or the Finite Element Method. In the approach taken in this work, the beam is discretized into a set of rays and the obscurant cloud as a set of scattering particles (Fig. 1). Even in the case where this clear separation of length scales is not present, this model still provides valuable information on the propagation of the beam and the reflected response of the dispersed system.³ An efficient discrete ray-tracking algorithm is developed to track the propagation of rays into the system. Quantitative examples are given, focusing on concentrated optical beams, their subsequent propagation, reflection and transmitted obscurant cloud response. Parameter studies are

² Resolving diffraction (which ray theory is incapable of describing) is unimportant for the applications of interest.

³ It is important to emphasize the regimes of validity of such a model are where the particle scatterers and surface features are larger than visible light rays: $3.8 \times 10^{-7} \text{ m} \leq \lambda \leq 7.2 \times 10^{-7} \text{ m}$. Thus, the particles in this analysis are assumed to possess diameters larger than approximately 10^{-5} m ($10 \mu\text{m}$). For systems containing particulates smaller than this, one can simply use the model as a qualitative guide.

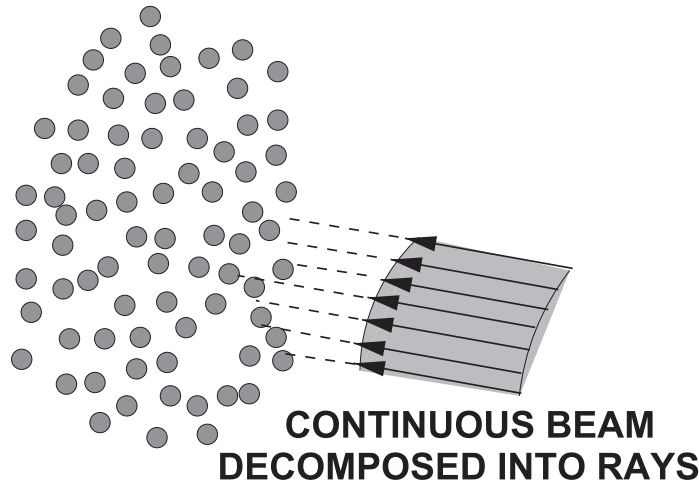


Fig. 2. Decomposition of an incoming beam into idealized “rays”.

conducted varying the randomly dispersed particles in the from spherical to oblate (flat, flake-like) scatterers and correlations are drawn between the overall scattering response of the cloud and the total amount of volume and surface area material available.

Remark 1. The work is further motivated by the advances, within the last few decades, in the development of optically-based imaging technologies, such as Light Detection And Ranging (LIDAR)-type technologies. LIDAR is a technique by which a target is illuminated with a laser and the reflected light is analyzed. LIDAR was developed in the 1960’s and combines laser focusing with radar-like technology for calculating distances by measuring time to for signal return. It is a relatively standard tool in the atmospheric sciences, ranging from remote sensing, airborne laser mapping and cloud measurement, and has been extended to a variety of applications in engineering and science. It has also started finding usage in the characterization of intentionally released obscurant clouds. Typically, LIDAR uses high-frequency ultraviolet, visible and near infrared light. For reviews, we refer the reader to Ring (1963), Cracknell and Hayes (2007), Goyer and Watson (1963) and Medina, Gaya, and Pozo (2006). Recently, there have also been efforts in developing obscurant penetrating/filtering LIDAR (Trickey, Church, & Cao, 2013).⁴

Remark 2. Over the years, a variety of other types of (non-particulate) obscurants have been developed for larger electromagnetic wavelength regimes. This type of obscurant is usually referred to as chaff. For example, in world war II, strips of aluminum were dumped from planes to confuse radar (Churchill, 1951; Jones, 1978) and modern variants are used for protection against missiles.

2. Propagation of electromagnetic energy

Following a framework found in Zohdi (2006a, 2006b, 2007), we consider a beam of light incident upon a material interface which produces a reflected wave and a transmitted (refracted) wave (Fig. 2), the amount of incident electromagnetic energy (I_i) that is reflected (I_r) is given by the total reflectance $IR \stackrel{\text{def}}{=} \frac{I_r}{I_i}$, where $0 \leq IR \leq 1$. IR is given by Eq. (2.1), for unpolarized electromagnetic radiation, where \hat{n} is the ratio of the refractive indices of the ambient (incident) medium (n_i) and transmitted medium (n_t), $\hat{n} = n_t/n_i$, where $\hat{\mu}$ is the ratio of the magnetic permeabilities of the surrounding incident medium (μ_i) and transmitted rod-like medium (μ_t), $\hat{\mu} = \mu_t/\mu_i$. We consider applications where the magnetic permeability is, within experimental measurements, virtually the same for both the matrix and rod phases. Thus, for the remainder of the work, we shall take $\hat{\mu} = 1$ ($\mu_o = \mu_i = \mu_t$) and, thus, $\hat{n} = \frac{n_t}{n_i} = \sqrt{\frac{\epsilon_t \mu_t}{\epsilon_i \mu_i}} \Rightarrow \epsilon_t \mu_t = (\hat{n})^2 \epsilon_i \mu_i \Rightarrow \epsilon_t = (\hat{n})^2 \epsilon_i$, where $\epsilon_i = \epsilon_o$.

For a beam of light, the reflectivity IR can be shown to be (see Gross, 2005 for example)

$$IR = \frac{I_r}{I_i} = \frac{1}{2} \left(\left(\frac{\frac{\hat{n}^2}{\hat{\mu}} \cos \theta_i - (\hat{n}^2 - \sin^2 \theta_i)^{\frac{1}{2}}}{\frac{\hat{n}^2}{\hat{\mu}} \cos \theta_i + (\hat{n}^2 - \sin^2 \theta_i)^{\frac{1}{2}}} \right)^2 + \left(\frac{\cos \theta_i - \frac{1}{\hat{\mu}} (\hat{n}^2 - \sin^2 \theta_i)^{\frac{1}{2}}}{\cos \theta_i + \frac{1}{\hat{\mu}} (\hat{n}^2 - \sin^2 \theta_i)^{\frac{1}{2}}} \right)^2 \right), \tag{2.1}$$

⁴ Generally, LIDAR bears some similarity with particle image velocimetry technologies.

where I_i is the incoming irradiance, I_r the reflected irradiance, n is the ratio of the refractive indices of the of transmitted (n_t) and incident media (n_i), where the refractive index is defined as the ration of the speed of light in a vacuum (c) to that of the medium (v), where the speed of electromagnetic waves is $c = \frac{1}{\sqrt{\epsilon_0 \mu_0}}$, where ϵ is the electric permittivity and μ is the magnetic permeability. All electromagnetic radiation travels, in a vacuum, at the speed $c \approx 2.99792458 \times 10^8 \pm 1.1$ m/s. In any another medium $v = \frac{1}{\sqrt{\epsilon \mu}}$ for electromagnetic waves.⁵ Notice that as $\hat{n} \rightarrow 1$ we have complete absorption, while as $\hat{n} \rightarrow \infty$ we have complete reflection. The total amount of absorbed power by the material is $(1 - IR)I_i$. The angle between the point of contact of a beam (Fig. 1) and the outward normal to the surface at that point is the angle of incidence (θ_i).

The classical reflection law states that the angle at which a beam is reflected is the same as the angle of incidence and that the incoming (incident, θ_i) and outgoing (reflected, θ_r) beam lays in the same plane, and $\theta_i = \theta_r$. Furthermore, refraction law states that, if the beam passes from one medium into a second one (with a different index of refraction), and, if the index of refraction of the second medium is less than that of the first, the angle the ray makes with the normal to the interface is always less than the angle of incidence, where $n \stackrel{\text{def}}{=} \frac{c}{v} = \sqrt{\frac{\epsilon \mu}{\epsilon_0 \mu_0}} = \frac{\sin \theta_i}{\sin \theta_t}$, θ_t being the angle of the transmitted ray (Fig. 1), c is the propagation speed in a vacuum and v is the propagation speed in the incident medium.

Since I is the energy per unit area per unit time, if we multiply by the “cross-sectional” area of the ray (A^r), we obtain the energy associated with an entire beam by multiplying the irradiance by the cross-sectional area of a coherent beam, IA^b , where A^b is the cross-sectional area of the beam (comprising all of the rays). The energy for a ray in the beam is then given by $IA^r = IA^b/N_r$, where N_r is the number of rays in the beam (Fig. 2). The angle between the point of contact of a ray (Fig. 1) and the outward normal to the surface at that point is the angle of incidence (θ_i). The classical reflection law (“Snell’s Law”) states that the angle at which the ray is reflected is the same as the angle of incidence and that the incoming (incident, θ_i) and outgoing (reflected, θ_r) rays lay in the same plane, and that $\theta_i = \theta_r$. Furthermore, the refraction/absorption law states that, if the ray passes from one medium into a second one (with a different index of refraction) and, if the index of refraction of the second medium is less than that of the first, then the angle the ray makes with the normal to the interface is always less than the angle of incidence, where θ_a is the angle of the absorbed ray (Fig. 1), $n \stackrel{\text{def}}{=} \frac{c}{v} = \sqrt{\frac{\epsilon \mu}{\epsilon_0 \mu_0}} = \frac{\sin \theta_i}{\sin \theta_a}$, c is the propagation speed in a vacuum and v is the propagation speed in the incident medium. By using the classical Fresnel equations, one can also describe the changes in ray magnitude. For example if we consider a ray incident upon a boundary separating two different materials, which produces a reflected ray and an absorbed (refracted) ray (Fig. 1), the amount of incident electromagnetic energy (I_i) that is reflected (I_r) is given by the total reflectance $IR \stackrel{\text{def}}{=} \frac{I_r}{I_i}$, where $0 \leq IR \leq 1$, where IR is derived shortly, for unpolarized electromagnetic radiation, where \hat{n} is the ratio of the refractive indices of the ambient (incident) medium (n_i) and absorbing particle medium (n_a), $\hat{n} = n_a/n_i$, where $\hat{\mu}$ is the ratio of the magnetic permeabilities of the surrounding incident medium (μ_i) and absorbing particle medium (μ_a), $\hat{\mu} = \mu_a/\mu_i$. Although we present a relatively general formulation, later we will consider applications where the magnetic permeability is, within experimental measurements, virtually the same for both the surroundings and particle. In other words, later in the work, we shall take $\hat{\mu} = 1$ ($\mu_o = \mu_i = \mu_a$) and, thus, $\hat{n} = \frac{n_a}{n_i} = \sqrt{\frac{\epsilon_a \mu_a}{\epsilon_i \mu_i}} \Rightarrow \epsilon_a \mu_a = (\hat{n})^2 \epsilon_i \mu_i \Rightarrow \epsilon_a = (\hat{n})^2 \epsilon_i$, where $\epsilon_i = \epsilon_o$. We refer the reader to Gross (2005) and Zohdi (2006a, 2006b, 2007) for details.

3. Parametrization of the obscurant cloud particulate configurations, shapes and surface normals

The classical random sequential addition process (RSA, Widom, 1966) is used to place nonoverlapping particles randomly into the domain of interest. This technique is adequate for the dispersed systems of interest. However, if higher particle density (volume fractions) are desired, more sophisticated processes, such as the equilibrium-based Metropolis algorithm can be used. See Torquato (2002) for a detailed review of such methods. Furthermore, for much higher volume fractions, effectively packing (and “jamming”) particles to theoretical limits, a class of methods, based on simultaneous particle flow and growth, has been developed by Torquato (2002), Kansaal, Torquato, and Stillinger (2002), Donev, Cisse, et al. (2004), Donev, Stillinger, Chaikin, and Torquato (2004) and Donev, Torquato, and Stillinger (2005a, 2005b, 2005c).

A general way to characterize a wide variety of types of particles, which are not necessarily spherical, can be achieved by modifying the equation for a generalized “hyper”-ellipsoid (Fig. 3):

$$F \stackrel{\text{def}}{=} \left(\frac{|x - x_0|}{\mathcal{R}_1} \right)^{s_1} + \left(\frac{|y - y_0|}{\mathcal{R}_2} \right)^{s_2} + \left(\frac{|z - z_0|}{\mathcal{R}_3} \right)^{s_3} = 1, \quad (3.1)$$

where the s 's are exponents. Values of $s < 1$ produce nonconvex shapes, while $s > 2$ values produce “block-like” shapes. Furthermore, we can introduce particulate aspect ratio, defined by $\mathcal{A}_r \stackrel{\text{def}}{=} \frac{\mathcal{R}_1}{\mathcal{R}_2} = \frac{\mathcal{R}_1}{\mathcal{R}_3}$, where $\mathcal{R}_2 = \mathcal{R}_3$, $\mathcal{A}_r > 1$ for prolate geometries and $\mathcal{A}_r < 1$ for oblate shapes. The outward surface normals, \mathbf{n} , needed during the scattering calculations, are easy to

⁵ The free space electric permittivity is $\epsilon_o = \frac{1}{c^2 \mu_o} = 8.8542 \times 10^{-12}$ C N⁻¹ m⁻¹ and the free space magnetic permeability is $\mu_o = 4\pi \times 10^{-7}$ Wb A⁻¹ m⁻¹ = 1.2566×10^{-6} Wb A⁻¹ m⁻¹.

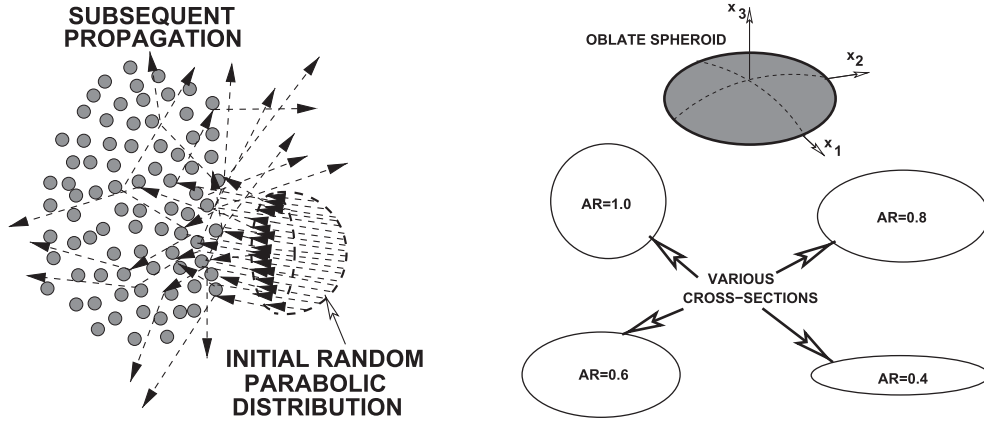


Fig. 3. LEFT: a laser pulse applied to a cloud material with parallel, randomly placed rays in the circular cross-sectional plane of the beam, corresponding to unpolarized incoming optical energy. The beam has an initial parabolic intensity that peaks at the centerline. RIGHT: various scatterer cross-sectional shapes used in the examples (progressively more oblate). The maximum radius is always kept the same for comparison purposes and the smaller radius is scaled by $A_r \leq 1$.

characterize by writing $\mathbf{n} = \frac{\nabla F}{\|\nabla F\|}$ with respect to a rotated frame that is aligned with the axes of symmetry of the generalized particle. The components of the gradient, $\nabla F = \frac{\partial F}{\partial x} \mathbf{e}_x + \frac{\partial F}{\partial y} \mathbf{e}_y + \frac{\partial F}{\partial z} \mathbf{e}_z$, are

$$\frac{\partial F}{\partial x} = \frac{1}{\mathcal{R}_1^{s_1}} \frac{\partial}{\partial x} \left(\sqrt{(x - x_0)^2} \right)^{s_1} = \frac{x s_1}{\mathcal{R}_1^{s_1}} \left(\sqrt{(x - x_0)^2} \right)^{s_1 - 2}, \tag{3.2}$$

and

$$\frac{\partial F}{\partial y} = \frac{1}{\mathcal{R}_2^{s_2}} \frac{\partial}{\partial y} \left(\sqrt{(y - y_0)^2} \right)^{s_2} = \frac{y s_2}{\mathcal{R}_2^{s_2}} \left(\sqrt{(y - y_0)^2} \right)^{s_2 - 2}, \tag{3.3}$$

and

$$\frac{\partial F}{\partial z} = \frac{1}{\mathcal{R}_3^{s_3}} \frac{\partial}{\partial z} \left(\sqrt{(z - z_0)^2} \right)^{s_3} = \frac{z s_3}{\mathcal{R}_3^{s_3}} \left(\sqrt{(z - z_0)^2} \right)^{s_3 - 2}. \tag{3.4}$$

The orientation of the particles, usually random, can be controlled, via standard rotational coordinate transformations, with random angles.

4. Model problem and response trends

From this point forth, we assume that the ambient and interstitial medium (surrounding the particles) behaves as a vacuum. Accordingly, there are no energetic losses as the rays move through the surrounding medium. Furthermore, we assume that absorbed portion of a ray that enters a particle are not re-emitted.

4.1. Tracking of beam decomposed rays

Starting at $t = 0$ and ending at $t = T$, the simple overall algorithm to track rays is as follows, at each time increment:

1. Check for intersections of rays with surfaces (hence a reflection), and compute the ray magnitudes and orientation if there are reflections (for all rays that are experiencing a reflection, $I_j^{ref}, j = 1, 2, \dots, Rays$).
2. Increment all ray positions ($\mathbf{x}_j(t + \Delta t) = \mathbf{x}_j(t) + \Delta t \mathbf{v}_j(t), j = 1, 2, \dots, Rays$).
3. Increment time forward ($t = t + \Delta t$) and repeat the process for the next time interval.

Observation 1. In order to capture all of the ray reflections that occur, the time step size Δt is dictated by the size of the particle scatterers. A somewhat ad hoc approach is to scale the time step size by the speed of the of ray propagation according to $\Delta t = \xi \frac{\mathcal{R}}{\|\mathbf{v}\|}$, where \mathcal{R} is the median radius of the particle scatterers (if the particle sizes are not uniform) and $0.05 \leq \xi \leq 0.1$. Typically, the results are insensitive to ξ that are smaller than this range. Although outside the scope of this work, one can also use this algorithm to compute the thermal response by combining it with heat transfer equations via staggering schemes (Zohdi, 2012a, 2012b, 2013).

Observation 2. For step (1), it is convenient to determine whether a ray has just entered a particle domain by checking if $F(\hat{x}, \hat{y}, \hat{z}) \leq 0$, where $(\hat{x}, \hat{y}, \hat{z})$ are the coordinates of the particle expressed in a rotated frame that is aligned with the axes of symmetry of the particle and then to compute the normal $\mathbf{n} = \frac{\nabla F}{\|\nabla F\|}$ in that frame.

Observation 3. There are a variety of options for simulation speed up involving ray-particle calculations. For example, one can construct a so-called *interaction list* of neighboring particles within a radius of influence with which a specific ray interacts for a few time steps. As the overall ray system configuration changes, one can periodically update the lists (see Pöschel & Schwager, 2004). For example, this dramatically reduces the computation time used in contact search, which is an N^2 operation. In this paper, we adopt the following process:

- An initial full-blown ray-particle contact search is initiated at the beginning of the simulation to generate an interaction list of nearest neighbors for each ray,
- The interaction lists are used for all ray-particle calculations for a select subinterval of the total simulation time, $0 \leq \Delta T \leq T$ and
- After a select subinterval of the total simulation time (ΔT) the interaction lists are updated for each ray. The checks are done only over the set of particles in a ray's interaction list.

Interaction lists were used throughout the upcoming simulations, with the results being tested against direct computation (no interaction truncation) in order to determine appropriate parameter settings for the truncation radius (typically 3–5 particle radii) and the frequency of list updating. The upcoming simulation results were insensitive to the truncations and are on the order of 50–100 times faster than direct computation.

Remark 1. One can also employ Domain Decomposition techniques whereby the domain is partitioned into subdomains, the particles within each subdomain are sent to a processor and stepped forward in time, but with the positions of the particles outside of the subdomain fixed (relative to the particles in that subdomain). This is done for all of the subdomains separately, then the position of all of the particles are updated and this information is shared between processors, with the procedure being repeated as needed. It is important to note that a significant acceleration in the computation can be achieved via sorting and binning methods, which proceed by partitioning the whole domain into bins. The particles are sorted by the bins in which they reside. The particle interaction proceeds, bin by bin, where the particles within a bin potentially only interact with particles in other nearest neighbor bins. Essentially, for a given particle in a bin, contact searches are conducted with particles in the neighboring bins only. The approach is relatively straightforward to implement and can speed up the computation significantly (see Zohdi, 2010, 2012b). There are a variety of related techniques to further accelerate computations. For example, one can assume that particles stay in the bins for a few time steps, and that one does not need to re-sort immediately. This can be also used in conjunction with interaction lists, although this was not done in this work.

Remark 2. For extremely large-scale systems, it is important to note that for the ray tracing method, there are two natural ways to proceed to exploit parallel computation: (1) By assigning each processor its share of the rays, and checking which particle scatterers interact with those rays or (2) By assigning each processor its share of particle scatterers, and checking which rays interact with those particle scatterers.

4.2. Quantitative examples

The discrete-ray/discrete-particle approach is flexible enough to simulate a wide variety of systems. As a model problem, we considered a group of N_p nonoverlapping randomly dispersed particles, of equal size in a cloud. The cloud was spherical with a cloud radius of $\mathcal{R}_c = 0.005$ m. We note that the size of the cloud and length-scale parameters can be adjusted easily to adapt to a desired specific application. The nondimensional ratio between the maximum particle radius (\mathcal{R}_p) and the cloud radius \mathcal{R}_c was denoted by $\mathcal{L} \stackrel{\text{def}}{=} \frac{\mathcal{R}_p}{\mathcal{R}_c}$. The initial velocity vector for all initially collinear rays comprising the beam was $\mathbf{v} = (c, 0, 0)$, where $c = 3 \times 10^8$ m/s is the speed of light in a vacuum. We used a refractive index ratio of $\hat{n} = 1.4$, for the set of particle scatterers. We steadily increased the number of rays in the beam from $N_r = 100, 200, \text{etc}$ until the results were insensitive to further refinements. This approach indicated that approximately $N_r = 2500$ parallel, but randomly placed within the beam, rays in the circular cross-sectional plane of the beam (Fig. 3), corresponding to unpolarized incoming optical energy yielded stable results across the parameter study range.⁶ Therefore, we consider the responses to be, for all practical purposes, independent of the ray density. This particle/ray system provided convergent results, i.e. increasing the number of rays and/or the number of particles surrounding the beam resulted in negligibly different overall system responses.⁷ In such a direct numerical approach, one can easily introduce nonuniform beam profiles such as shown in Fig. 1

⁶ We repeatedly refined the “ray density” up to 10000 rays and found no significant difference compared to the 2500 ray result.

⁷ In order to adequately compare between different tests in Table 1, the same random 2000 particle ensemble was used each time.

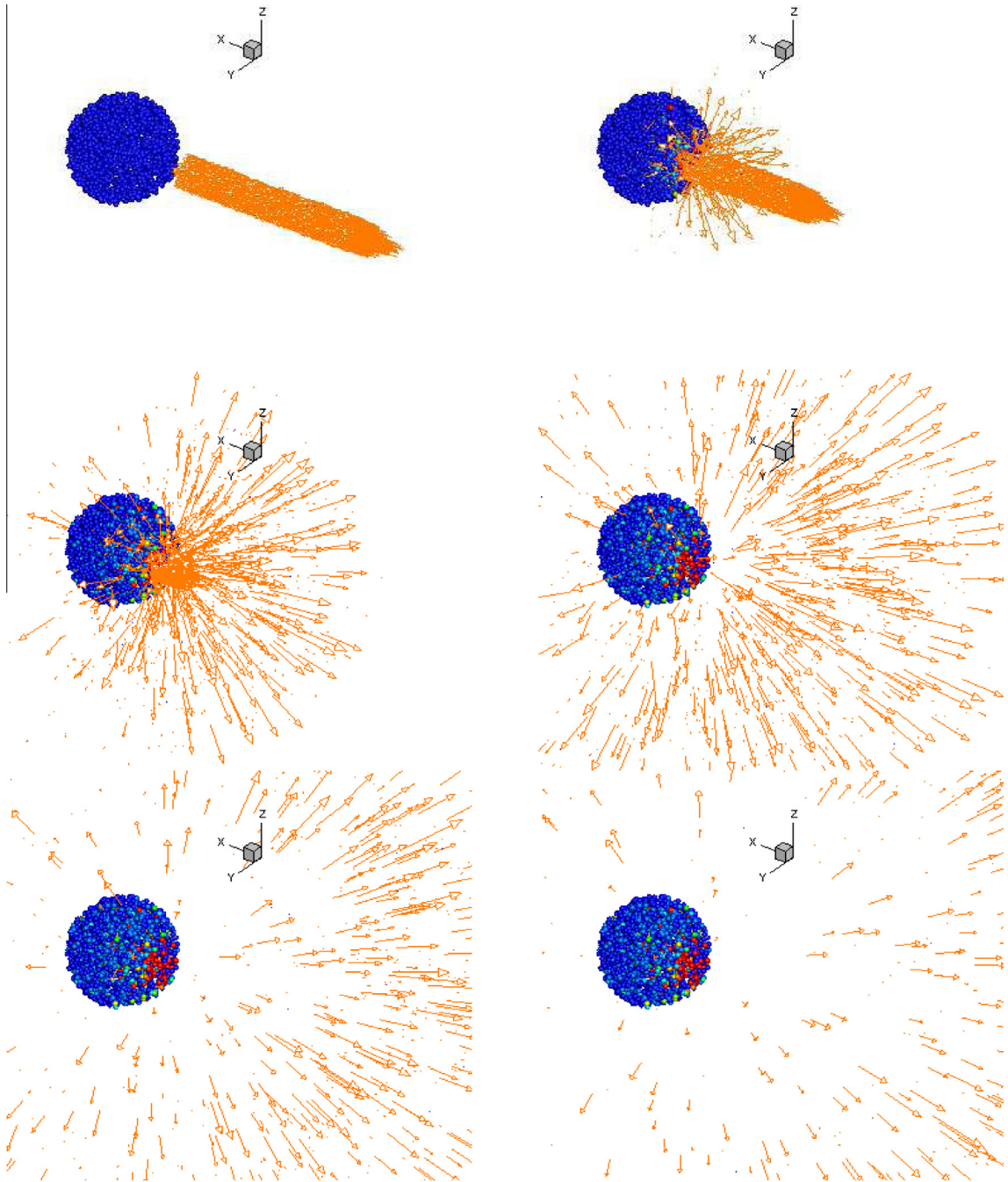


Fig. 4. Top to bottom and left to right: the detailed obscurant cloud (2000 randomly dispersed particle scatterers) response to 2500 rays. Typically, each ray will undergo, on average approximately 10–15 reflections in this system (roughly 25,000–40,000 total system reflections). The colors of the scatterers indicate the total amount of irradiance absorbed, normalized by the average irradiance of each ray initially in the beam. (For interpretation of the references to color in this figure legend, the reader is referred to the web version of this article.)

$$I(d) = I(d = 0)e^{-ad}, \quad (4.1)$$

where d is the distance from the center of the initial beam line. In the case of $a = 0$ we recapture a flat beam, $I(d) = I(d = 0)$. We specifically used $a = 2$. We set total initial irradiance via $\sum_{i=1}^{N_r} I_i^{inc}(t = 0) \mathcal{A}_r = P$ Watts.⁸ The radius of the beam was $0.3 \mathcal{R}_c$.

⁸ To achieve this distribution, we first placed rays randomly in the plane, and then scaled the individual I_i^{inc} by e^{-ad} and the normalized the average so that the total was P watts. The numerical value of P is not relevant, unless we consider heating, which is not the present case.

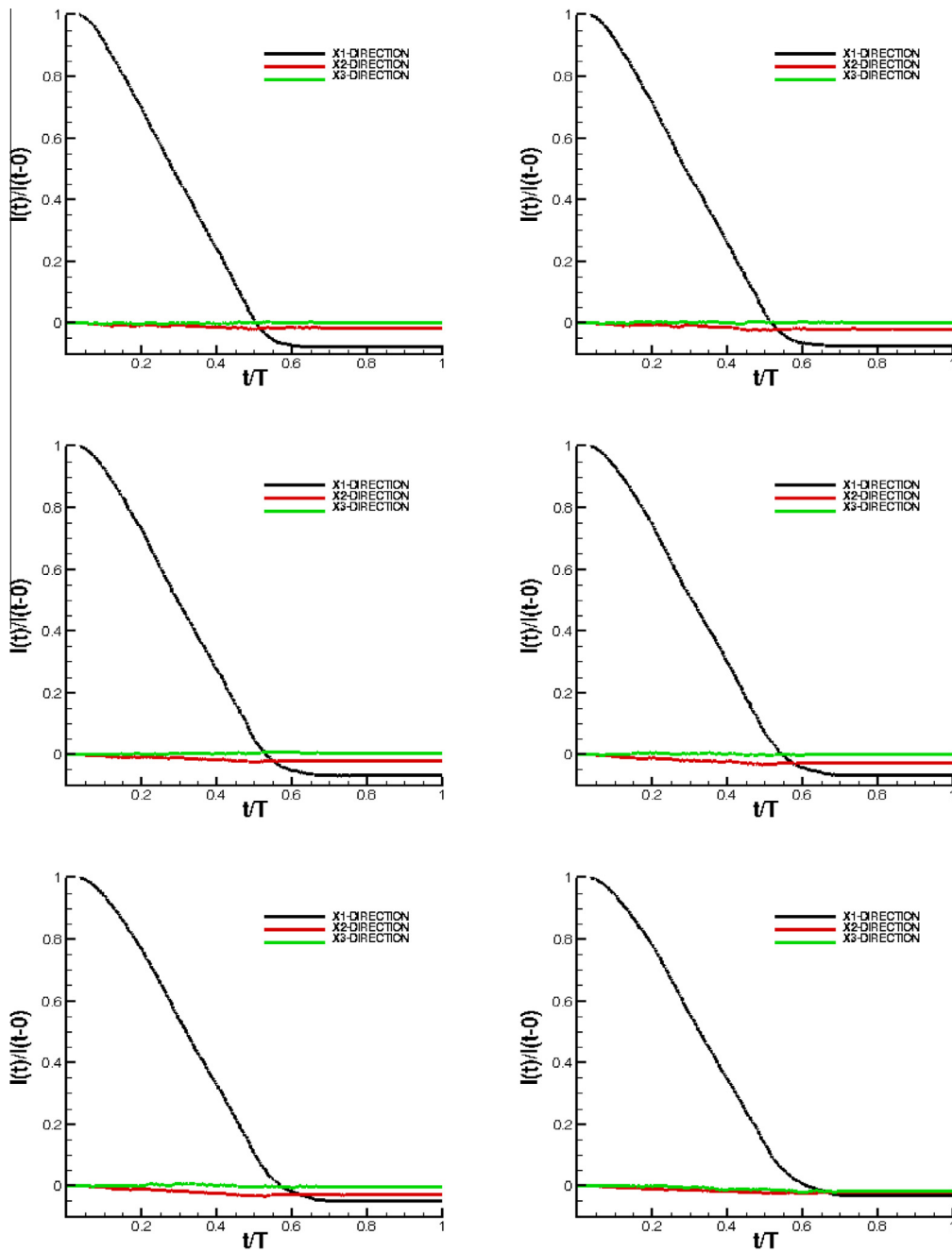


Fig. 5. Top to bottom and left to right: the decay curves of normalized energy content for the beam for progressively more oblate aspect ratios of $\mathcal{A}_r = 1, 0.8, 0.6, 0.4, 0.2$ and 0.1 .

4.3. Explanation of trends

We tabulated several metrics of the beam-cloud interaction response:

- Metric – 1: The normalized sum of all ray components in the x_1 -direction:
$$\frac{\sum_{i=1}^{rays} \mathbf{I}_i(t) \cdot \mathbf{e}_x}{\sum_{i=1}^{rays} \|\mathbf{I}_i(t=0)\|}$$
- Metric – 2: The normalized sum of all ray components in the x_2 -direction:
$$\frac{\sum_{i=1}^{rays} \mathbf{I}_i(t) \cdot \mathbf{e}_y}{\sum_{i=1}^{rays} \|\mathbf{I}_i(t=0)\|}$$
- Metric – 3: The normalized sum of all ray components in the x_3 -direction:
$$\frac{\sum_{i=1}^{rays} \mathbf{I}_i(t) \cdot \mathbf{e}_z}{\sum_{i=1}^{rays} \|\mathbf{I}_i(t=0)\|}$$

Table 1

The overall response, illustrated by metrics, *Metric – 1* through *Metric – 7*, to a 2500 rays for 2000 randomly dispersed particle scatterers after a sufficiently long time $t = T$, allowing all of the rays to have exited the scattering system ($\mathcal{L} = 0.05$). The max radius size was set to $\mathcal{R} = \mathcal{L}\mathcal{R}_c$. Note the reduction of the back scattering efficiency of flakes, which however, have significantly less mass, than spheres. From the point of view of being buoyant/airborne, clearly flakes are advantageous. The maximum radius is always kept the same for comparison purposes and the smaller radius is scaled by $\mathcal{A}_r \leq 1$.

\mathcal{A}_r	<i>Metric – 1</i>	<i>Metric – 2</i>	<i>Metric – 3</i>	<i>Metric – 4</i>	<i>Metric – 5</i>	<i>Metric – 6</i>	<i>Metric – 7</i>
1.0	–0.07812082	–0.01500523	0.00110415	0.00749938	0.03583117	0.04173188	0.17516937
0.8	–0.07410705	–0.01896547	0.00240142	0.00858968	0.03279774	0.04037649	0.17052205
0.6	–0.06695769	–0.01968796	0.00496642	0.01221877	0.03278525	0.04464278	0.17395373
0.4	–0.06657105	–0.02689264	0.00078536	0.01733303	0.03019442	0.04369102	0.18475583
0.2	–0.04827146	–0.02868155	–0.00131545	0.03373935	0.03196293	0.04760661	0.20388434
0.1	–0.03095679	–0.02099628	–0.01668062	0.05458418	0.03629362	0.04174643	0.22661932

- *Metric – 4*: The normalized sum of all ray components that are positive in the x_1 -direction: $\frac{\sum_{i=1}^{\text{rays}} \mathbf{I}_i(t) \cdot \mathbf{e}_x}{\sum_{i=1}^{\text{rays}} \|\mathbf{I}_i(t=0)\|}$, where $\mathbf{I}_i(t) \cdot \mathbf{e}_x \geq 0$.
- *Metric – 5*: The normalized sum of all ray components that are positive in the x_2 -direction: $\frac{\sum_{i=1}^{\text{rays}} \mathbf{I}_i(t) \cdot \mathbf{e}_y}{\sum_{i=1}^{\text{rays}} \|\mathbf{I}_i(t=0)\|}$, where $\mathbf{I}_i(t) \cdot \mathbf{e}_y \geq 0$.
- *Metric – 6*: The normalized sum of all ray components that are positive in the x_3 -direction: $\frac{\sum_{i=1}^{\text{rays}} \mathbf{I}_i(t) \cdot \mathbf{e}_z}{\sum_{i=1}^{\text{rays}} \|\mathbf{I}_i(t=0)\|}$, where $\mathbf{I}_i(t) \cdot \mathbf{e}_z \geq 0$.
- *Metric – 7*: The normalized sum of all ray magnitudes: $\frac{\sum_{i=1}^{\text{rays}} \|\mathbf{I}_i(t)\|}{\sum_{i=1}^{\text{rays}} \|\mathbf{I}_i(t=0)\|}$.

Fig. 4 shows a sequence of frames of the detailed response of an obscurant cloud (2000 randomly dispersed particle scatterers) to 2500 rays. Typically, each ray will undergo, on average approximately 10–15 reflections in this system (roughly 25,000–40,000 total system reflections). The colors of the scatterers indicate the total amount of irradiance absorbed, normalized by the average irradiance of each ray initially in the beam. Fig. 5 shows the plots of the irradiance content (decay) of the beam as in encounters the cloud, for various particle types.

5. Discussion and summary

As Table 1 shows, there is a reduction of the back scattering efficiency of flakes (relative to spheres), which however, have significantly less mass, than spheres. Thus, there is a trade-off between the mass in the system and the scattering efficiency. The ratio of masses between a baseline sphere and ellipsoid, as well as the special case of oblate spheroids considered are:

$$\frac{M_{oe}}{M_s} = \frac{\rho \frac{4}{3} \pi \mathcal{R}_1 \mathcal{R}_2 \mathcal{R}_3}{\rho \frac{4}{3} \pi \mathcal{R}^3} = \frac{\mathcal{A}_r \mathcal{R}^3}{\mathcal{R}^3} = \mathcal{A}_r. \tag{5.1}$$

Therefore, the total amount of mass available to interact with the beam is significantly smaller. However, the reduction of surface area is far less dramatic. There is no general closed form formula for an ellipsoid (some approximate forms exist in terms of incomplete elliptic integrals of the first and second kind).⁹ However, in order to obtain simple qualitative estimates, consider an approximation of a sphere collapsed to a thin disc of height $h \approx \mathcal{A}_r \mathcal{R}$. The surface area ratio of the oblate ellipsoid and a sphere is:

$$\frac{S_{oe}}{S_s} = \frac{2(\pi h \mathcal{R} + \pi \mathcal{R}^2)}{4\pi \mathcal{R}^2} = \frac{2(\pi \mathcal{A}_r \mathcal{R}^2 + \mathcal{R}^2)}{4\pi \mathcal{R}^2} = \frac{2(\mathcal{A}_r + 1)}{4} = \frac{(\mathcal{A}_r + 1)}{2}. \tag{5.2}$$

Thus, one would expect, for example, the relative change in forward/backscatter, essentially the ratio of *Metric – 1* for ellipsoids and spheres, $\frac{(Metric-1)^{oe}}{(Metric-1)^s}$ to lay between

$$\mathcal{A}_r \leq \frac{(Metric - 1)^{oe}}{(Metric - 1)^s} \leq \frac{(\mathcal{A}_r + 1)}{2}, \tag{5.3}$$

which is the case in the tabulated results.

In summary, this work developed a discrete-ray/discrete-particle model to allow for propagation of optical energy through a cloud of randomly dispersed particles forming an obscurant. The approach provides a simpler alternative to a direct computationally intensive discretization of a continuum description employing Maxwell’s equations. Because of the complex microstructure, containing gaps and interfaces, this type of system is extremely difficult to simulate using continuum-based methods, such as the Finite Difference Time Domain Method or the Finite Element Method. The approach allows one to parametrically study the changes in scattering behavior as a function of changes in geometry such as from strongly oblate spheroids (flakes) to spheres, and to correlate this to mass and surface area of the scatterers. The simplified model captures the primary effects, namely, reflection and absorption of optical energy via: (1) a discrete element representation of the obscurant

⁹ More precise expressions for the surface area of an ellipsoid can be found in [Olver, Lozier, Boisvert, and Clark \(2010\)](#).

particle system (2) a discretization of a concentrated optical beam into rays and (3) a discrete ray-tracking algorithm is developed to track the propagation of rays. *The simulations take on the order of two minutes on a laptop.* As mentioned in the beginning of the paper, the regimes of validity of such a model are where the particle scatterers and surface features are larger than visible light rays: $3.8 \times 10^{-7} \text{ m} \leq \lambda \leq 7.2 \times 10^{-7} \text{ m}$. The particles in this analysis were assumed to possess diameters larger than approximately 10^{-5} m ($10 \mu\text{m}$). For systems with particulates smaller than this, one can interpret the results of the model in a qualitative manner, although the range of applicability is not limited to visible frequencies. Other high frequency applications where the developed model can be employed include UV-rays, X-rays, gamma rays and correspondingly smaller particle scatterer sizes, such as (a) regimes where the scatterers and surface features are larger than ultraviolet rays ($10^{-9} \text{ m} \leq \lambda \leq 10^{-8} \text{ m}$), (b) regimes where the scatterers and surface features are larger than X-rays ($10^{-11} \text{ m} \leq \lambda \leq 10^{-9} \text{ m}$), and (c) regimes where the scatterers and surface features are larger than gamma-rays ($10^{-12} \text{ m} \leq \lambda \leq 10^{-11} \text{ m}$).

Acknowledgements

This work was funded in part by the Army Research Laboratory through the Army High Performance Computing Research Center (cooperative agreement W911NF-07-2-0027).

References

- Avcı, B., & Wriggers, P. (2012). A DEM–FEM coupling approach for the direct numerical simulation of 3D particulate flows. *Journal of Applied Mechanics*, 79, 010901–(1–7).
- Bolintineanu, D. S., Grest, G. S., Lechman, J. B., Pierce, F., Plimpton, S. J., & Schunk, P. R. (2014). Particle dynamics modeling methods for colloid suspensions. *Computational Particle Mechanics*, 1(3), 321–356.
- Cabalo, J., Schmidt, J., Wendt, J. O. L., & Scheeline, A. (2002). Spectrometric system for characterizing drop and powder trajectories and chemistry in reactive flows. *Applied Spectroscopy*, 56, 1346–1353.
- Cante, J., Davalos, C., Hernandez, J. A., Oliver, J., Jonsen, P., Gustafsson, G., et al (2014). PFEM-based modeling of industrial granular flows. *Computational Particle Mechanics*, 1(1), 47–70.
- Carbonell, J. M., Onate, E., & Suarez, B. (2010). Modeling of ground excavation with the particle finite element method. *Journal of Engineering Mechanics, ASCE*, 136, 455–463.
- Churchill, W. S. (1951). *The second world war: Closing the ring*. Boston: Houghton Mifflin Company, p. 64.
- Cracknell, A. P., & Hayes, L. (2007). *Introduction to remote sensing* (2 ed.). London: Taylor and Francis. ISBN 0-8493-9255-1. OCLC 70765252.
- Donev, A., Cisse, L., Sachs, D., Vaziano, E. A., Stillinger, F., & Connelly, R. (2004). Improving the density of jammed disordered packings using ellipsoids. *Science*, 303, 990–993 (13 February 2004).
- Donev, A., Stillinger, F. H., Chaikin, P. M., & Torquato, S. (2004). Unusually dense crystal ellipsoid packings. *Physical Review Letters*, 92, 255506.
- Donev, A., Torquato, S., & Stillinger, F. (2005a). Neighbor list collision-driven molecular dynamics simulation for nonspherical hard particles-I. Algorithmic details. *Journal of Computational Physics*, 202, 737.
- Donev, A., Torquato, S., & Stillinger, F. (2005b). Neighbor list collision-driven molecular dynamics simulation for nonspherical hard particles-II. Application to ellipses and ellipsoids. *Journal of Computational Physics*, 202, 765.
- Donev, A., Torquato, S., & Stillinger, F. H. (2005c). Pair correlation function characteristics of nearly jammed disordered and ordered hard-sphere packings. *Physical Review E*, 71, 011105.
- Duran, J. (1997). *Sands, powders and grains. An introduction to the physics of granular matter*. Springer Verlag.
- Goyer, G. G., & Watson, R. (1963). The laser and its application to meteorology. *Bulletin of the American Meteorological Society*, 44(9), 564575 [568].
- Gregoire, Y., Sturzer, M. -O., Khasainov, B. A., & Veyssiere, B. (2009). Investigation of the behavior of solid particles dispersed by high explosive. In *40th international annual conference of the ICT*, 35/1–35/12.
- Gross, H. (2005). Handbook of optical systems. In H. Gross (Ed.), *Fundamental of technical optics*. Wiley-VCH.
- Hoover, W. G., & Hoover, C. G. (2009). Tensor temperature and shock-wave stability in a strong two-dimensional shock wave. *Physical Review E: Statistical, Nonlinear, and Soft Matter Physics*, 80, 011128/1–011128/6.
- Jones, R.V. (1978). *Most secret war: British scientific intelligence 1939–1945*. Hamish Hamilton, London. ISBN 0-241-89746-7.
- Kansaal, A., Torquato, S., & Stillinger, F. (2002). Diversity of order and densities in jammed hard-particle packings. *Physical Review E*, 66, 041109.
- Kudryashova, O. B., Vorozhtsov, B. I., Muravlev, E. V., Akhmadeev, I. R., Pavlenko, A. A., & Titov, S. S. (2011). Physicomathematical modeling of explosive dispersion of liquid and powders. *Propellants, Explosives, Pyrotechnics*, 36, 524–530.
- Labra, C., & Onate, E. (2009). High-density sphere packing for discrete element method simulations. *Communications in Numerical Methods in Engineering*, 25(7), 837–849.
- Leonardi, A., Wittel, F. K., Mendoza, M., & Herrmann, H. J. (2014). Coupled DEM–LBM method for the free-surface simulation of heterogeneous suspensions. *Computational Particle Mechanics*, 1(1), 3–13.
- Medina, A., Gaya, F., & Pozo, F. (2006). Compact laser radar and three-dimensional camera. *The Journal of the Optical Society of America A*, 23, 800805.
- Olver, F. W. J., Lozier, D. W., Boisvert, R. F., & Clark, C. W. (2010). *NIST handbook of mathematical functions*. Cambridge University Press.
- Onate, E., Celiueta, M. A., Idelsohn, S. R., Salazar, F., & Surez, B. (2011). Possibilities of the particle finite element method for fluid–soil–structure interaction problems. *Computational Mechanics*, 48, 307–318.
- Onate, E., Celiueta, M. A., Latorre, S., Casas, G., Rossi, R., & Rojek, J. (2014). Lagrangian analysis of multiscale particulate flows with the particle finite element method. *Computational Particle Mechanics*, 1(1), 85–102.
- Onate, E., Idelsohn, S. R., Celiueta, M. A., & Rossi, R. (2008). Advances in the particle finite element method for the analysis of fluid–multibody interaction and bed erosion in free surface flows. *Computer Methods in Applied Mechanics and Engineering*, 197(19–20), 1777–1800.
- Pöschel, T., & Schwager, T. (2004). *Computational granular dynamics*. Springer Verlag.
- Ring, J. (1963). *The laser in astronomy*. New Scientist, p. 672–3.
- Rojek, J. (2014). Discrete element thermomechanical modelling of rock cutting with valuation of tool wear. *Computational Particle Mechanics*, 1(1), 71–84.
- Rojek, J., Labra, C., Su, O., & Onate, E. (2012). Comparative study of different discrete element models and evaluation of equivalent micromechanical parameters. *International Journal of Solids and Structures*, 49, 1497–1517. <http://dx.doi.org/10.1016/j.ijsolstr.2012.02.032>.
- Torquato, S. (2002). *Random heterogeneous materials: Microstructure & macroscopic properties*. New York: Springer-Verlag.
- Trickey, E., Church, P., & Cao, X. (2013). Characterization of the OPAL obscurant penetrating LiDAR in various degraded visual environments. In *Proc. SPIE 8737, degraded visual environments: Enhanced, synthetic, and external vision solutions 2013*, 87370E (16 May 2013); doi: 10.1117/12.2015259.
- Widom, B. (1966). Random sequential addition of hard spheres to a volume. *Journal of Chemical Physics*, 44, 3888–3894.
- Zohdi, T. I. (2004). A computational framework for agglomeration in thermo-chemically reacting granular flows. *Proceedings of the Royal Society*, 460(2052), 3421–3445.

- Zohdi, T. I. (2005). Charge-induced clustering in multifield particulate flow. *The International Journal of Numerical Methods in Engineering*, 62(7), 870–898.
- Zohdi, T. I. (2006a). On the optical thickness of disordered particulate media. *Mechanics of Materials*, 38, 969–981.
- Zohdi, T. I. (2006b). Computation of the coupled thermo-optical scattering properties of random particulate systems. *Computer Methods in Applied Mechanics and Engineering*, 195, 5813–5830.
- Zohdi, T. I. (2007). Computation of strongly coupled multifield interaction in particle–fluid systems. *Computer Methods in Applied Mechanics and Engineering*, 196, 3927–3950.
- Zohdi, T. I. (2010). On the dynamics of charged electromagnetic particulate jets. *Archives of Computational Methods in Engineering*, 17(2), 109–135.
- Zohdi, T. I. (2012a). *Electromagnetic properties of multiphase dielectrics. A primer on modeling, theory and computation*. Springer-Verlag.
- Zohdi, T. I. (2012b). *Dynamics of charged particulate systems. Modeling, theory and computation*. Springer-Verlag.
- Zohdi, T. I. (2013). Numerical simulation of charged particulate cluster-droplet impact on electrified surfaces. *Journal of Computational Physics*, 233, 509–526.
- Zohdi, T. (2014). Embedded electromagnetically sensitive particle motion in functionalized fluids. *Computational Particle Mechanics*, 1(1), 27–45.

Further reading

- Jackson, J. D. (1998). *Classical electrodynamics* (3rd ed.). Wiley.
- Zohdi, T. I., & Kuypers, F. A. (2006). Modeling and rapid simulation of multiple red blood cell light scattering. *Proceedings of the Royal Society Interface*, 3(11), 823–831.